Ravi, S. K., Paul, N., Salim, A. T., Wu, T., Wu, Z., Jones, M. R., & Tan, S. C. (2019). Bio-photocapacitive Tactile Sensors as a Touch-to-Audio Braille Reader and Solar Capacitor. *Materials Horizons*. https://doi.org/10.1039/c9mh01798d

Bio-photocapacitive Tactile Sensors as a Touch-to-Audio Braille Reader and Solar Capacitor

Sai Kishore Ravi[1†], Nikita Paul[1†], Lakshmi Suresh[1 †], Aditya Tjitra Salim[1†], Tingfeng Wu[1], Zixuan Wu[2], Michael R. Jones[3], Swee Ching Tan[1]*

†The authors contributed equally to the work

[1]Department of Materials Science and Engineering, National University of Singapore, 9 Engineering Drive 1, Singapore 117575.

[2]Department of Materials Science and Engineering, University of Illinois at Urbana-Champaign, 1304 W Green St, Urbana, IL 61801, USA.

[3]School of Biochemistry, University of Bristol, Biomedical Sciences Building, University Walk, Bristol BS8 1TD, United Kingdom.

*Correspondence to: msetansc@nus.edu.sg

Abstract

Human-machine interfaces in emerging smart-skin technologies tend to be focussed towards high-sensitivity tactile sensing primarily with visual/numerical feedback, and research on e-skin technologies for the visually impaired is sparse. Here we demonstrate a proof-of-concept six-pixel tactile sensor that converts touch stimuli based on Braille codes into an auditory output, and which could potentially be miniaturized as an 'energy-autonomous on-skin e-Braille reader' for the visually impaired. By applying the concepts of electric double layer capacitance and bio-photo capacitance, a self-powered sensor is constructed that generates electrical signals as large as 2 V by modulating a bio-electrochemical liquid bridge between electrodes of opposite wetting characteristics. The liquid bridge, composed of photosynthetic pigment-proteins with a redox electrolyte, both augments the sensory response and serves as a standalone solar-capacitor that can generate a photocurrent as high as 140 μA cm^{-2}, and which displays a long discharge time of ~20 mins with just ~3 mins of photo charging.

Introduction

Human-machine interaction[1-3] has in recent years reached new heights of advancement in technologies for areas as diverse as bio-medical[4-6], military[7,8], automotives[9,10] and consumer electronics[11,12], fuelling a huge growth particularly in the global market for wearable electronics[13]. Electronically emulating the human senses of tactility, vision, olfaction, audition, and gustation in perceiving changes in the surrounding environment and translating the cues back into human-understandable forms presents a grand challenge in the design of intelligent human-machine interfaces (HMIs). Most HMIs emulate at least one of the six senses in perceiving and interpreting external stimuli and return one or more forms of human-understandable signals, most commonly in a visual form[14,15]. Tactile sensing is central to most HMIs[16-18]; touchscreen displays in smartphones, computers and smart watches are good examples of basic tactile sensing with visual feedback.

Beyond mere sensing of touch or applied pressure, the idea of tactile sensing has gained new dimensions in emergent technologies such as electronic skins, where the need is to develop a robotic equivalent to human skin. Besides simple pressure-sensing, the concept of artificial skin demands a more complex set of functionalities such as the achievement of ultrahigh pressure sensitivity, fast response times, the capability to differentiate between multiple types of tactile stimuli (e.g. static pressure, dynamic pressure, strain, vibration etc.) and the ability to discern surface textures[19-21]. Skin-inspired tactile sensors[22,23] have promising applications in humanoid robotics[24], skin prosthetics[25,26], body-attachable[27] or on-skin electronic devices[28,29], and in unobtrusive health monitors[30]. Significant research effort has been devoted to developing smart tactile sensors for varied applications employing different principles of sensing such as capacitive pressure sensing[31,32], piezoresistivity[33,34], piezoelectricity[35,36], piezotronics[37-39], triboelectricity[40], tribotronics[41,42] and pressure-sensing with field-effect transistors[31,43,44].

As the vast majority of tactile sensors described in the literature are skin-inspired, research has been largely limited to detecting, differentiating and quantifying external physical stimuli. Most reports on tactile sensing stop at the quantification of stimuli such as pressure or temperature in terms of a proportionate change in an electrical signal such as voltage, resistance or capacitance. While HMIs are ideally required to be bidirectional (i.e. with both sensing and feedback functions), the primary focus has been on tactile sensing and research on different possible forms of sensory feedback is still relatively sparse. A few comprehensive reports on

tactile sensing for prosthetic and bio-medical applications have addressed aspects of sensory feedback with some attempts to directly deliver sensory feedback to brain[15,26]. Going a step further from the numerical quantification of stimuli, a few works have demonstrated practical visual interpretation of the collected sensory data by means of real-time pressure mapping[45,46] and wireless transmission of the visual feedback to phones or computers[2,34,47,48]. However, there has been relatively little research of applications requiring sensory feedback beyond visual interpretation, the addressing of which forms the primary subject of this work.

Herein, we demonstrate a proof-of-concept tactile sensing model that provides auditory feedback as a processed output in response to a touch stimulus (**Figure 1A**). For bidirectional communication between a machine and a human to be effective, cues feeding more than one of the six senses is often required. Alternative or complementary feedback is often required in HMIs where a visual-display capability is not feasible. Examples are in HMIs involving users in motion, engaged in navigation or where there are other demands on visual attention (where to pay attention to a visual cue from the machine would not be possible) and in HMIs involving users with special needs such as visual impairment or dyslexia. Although there has not been any study of auditory feedback in tactile sensing smart-skins or e-skins, studies on computer vision and gesture sensing have evaluated the benefits of the use of auditory feedback instead of, or along with, visual feedback[49,50], the basic arguments of which still hold good for tactile sensors. A simple example in the context of tactile sensors could be pressure sensing in a fitness/wellness tracker or a jogging shoe insole where an audio warning to alert the user of any abnormal pressure distribution could be of greater utility than the visual display of a pressure distribution map. However, the touch-to-audio conversion demonstrated in this work focusses on HMIs for the visually impaired, the proof-of-concept device using a six-pixel tactile sensor that matches the six dots in a basic Braille character set to translate touch in different Braille patterns to an audio signal that pronounces the corresponding letter. This model provides proof-of-concept for an 'on-skin e-Braille reader' that could be mounted on the user's fingertip such that the device can translate and read out the Braille text as one touches the text containing defined patterns of surface projections, sharing the output with others A comparison of similar strategies available for tactile sensing is summarised in **Table S1**.

To explore this concept a six-pixel bio-photo capacitive tactile sensor (**Figure 1B**) was constructed with each pixel holding a bio-electrochemical liquid bridge between two electrodes of opposite wetting characteristics (**Figure 1C, D**). The liquid bridge was composed of a

mixture of a concentrated solution of natural reaction centre/light harvesting 1 (RC-LH1) pigment-protein complexes from a photosynthetic bacterium (**Figure 1E**) and the ferrocyanide/ferricyanide redox couple. This combination was used to address a major problem in most skin-inspired tactile sensors where the lack of an inherent energy harvesting element to power the sensors' functions limits their practicality. Though a number of self-powered tactile sensors have been reported, the power generated is often not a stable continuous supply but rather is transient and pulsated. Annexing flexible batteries and supercapacitors with tactile sensors has been thought of as a solution, but issues such as health/environmental hazards from materials used in batteries/capacitors and the limited usage duration (or need to recharge) necessitates a non-hazardous *in-situ* power source in sensors. Naturally-sourced RC-LH1 pigment-protein complexes provide a viable and sustainable material to both enhance and power sensory functions by harvesting energy from ambient indoor light or sunlight. Although considered applications of photosynthetic proteins has been primarily limited to bio-photovoltaics and photoelectrochemical cells[51-67], the possibility of employing such complexes to power the sensory actions in e-skins has been presented in previous work from our laboratories[68]. In the present report, we demonstrate the possibility of using a new type of bio-hybrid microfluidic device both as a tactile sensor and as a standalone photo capacitor. This is achieved by both optically and mechanically manipulating the electric double layer capacitors (EDLCs) formed at the two electrolyte/electrode interfaces in the device. While photo-induced charge-separation in the RC-LH1 proteins charges the EDLCs, making them photo-capacitive, the touch stimulus alters the capacitance at either interface as the liquid bridge is asymmetrically compressed between the hydrophobic and hydrophilic electrodes. In response to touch, the device generated electrical signals as high as 2 V and upon 1 Sun illumination it generated a photocurrent of 140 μA cm^{-2} with an ideal photo capacitive behaviour of -20 mins discharge time for -3 mins of photo charging. The 2 V touch response is more than 100-fold higher than that of a previous comparable EDLC-based tactile sensor[69].

Results and Discussion

Device design and fabrication

The design of the tactile sensor was based on that of a microfluidic capacitive device[70-72], with an ionic liquid droplet between two flexible conductive electrodes. The primary structure of the six-pixel device comprised six polydimethylsiloxane (PDMS) wells to hold six discrete droplets. A mould with six protrusions was 3D printed from acrylonitrile butadiene styrene (ABS) (Supplementary information, **Figure S1A**). Strips of copper foil were adhered to each protrusion before pouring a mixture of PDMS and curing agent. Thermal curing resulted in a PDMS sheet approximately 2.5 mm thick with six wells. After removing the ABS mould the Cu foil exposed at the bottom of each well was coated with ≈200 nm of ITO by sputtering through a mask, and an ionic droplet of 3 µL protein/electrolyte mixture was then added to each well. A flexible sheet of indium tin oxide coated polyethylene terephthalate (ITO/PET) treated with 1H,1H,2H,2H-perfluorodecyltriethoxysilane (PFDTS) was then adhered to the cast PDMS structure to act as a single common top electrode to the six pixels. The PFDTS treatment made the top ITO electrode hydrophobic to maintain the shape of the droplet after deformation (due to touch/force applied) by preventing adherence, whilst by use of Cu foil as the substrate for ITO sputtering the bottom electrode was made hydrophilic to pin the droplet at a fixed position. The wetting characteristics of the top electrode were optimized using different variants of a surface treatment protocol (**Figure S2 and Note 1 in** Supplementary Information). The ionic droplet was composed of an equimolar $K_3[Fe(CN)_6]/K_4[Fe(CN)_6]$ redox electrolyte either as the sole component or mixed with a concentrated solution of RC-LH1 pigment-protein. This droplet formed a bioelectrochemical liquid bridge between the hydrophobic and hydrophilic electrodes (**Figure 1 C-D**). The RC-LH1 proteins (**Figure 1 E**)were isolated from the purple photosynthetic bacterium *Rhodobacter sphaeroides* (Supplementary information, **Figure S3A**); this protein absorbs light in the wavelength range of 200 - 950 nm and converts absorbed solar energy into a trans-protein electrical potential difference (Supplementary information, **Figure S3B**).

Tactile sensing characteristics

The electrical responses to touch stimuli were recorded by compressing the bioelectrochemical liquid bridge in a single pixel. To test different droplet compositions, several equimolar

solutions of $K_3[Fe(CN)_6]/K_4[Fe(CN)_6]$ between 5 and 400 mM were prepared and the touch response was recorded without and with the addition of proteins. For a droplet composed of 5 mM $K_3[Fe(CN)_6]/K_4[Fe(CN)_6]$ without any protein, the application of an instantaneous force by touch (≈7.84 N) resulted in a forward peak voltage of ≈0.1 V (average: 0.08 V) followed by a reverse peak voltage of ≈0.15 V (**Figure 2A**). A similar trend with forward and reverse peaks was also observed in the current response (Supplementary information, **Figure S4**). For a droplet formed form a 1:1 (v:v) mixture of concentrated RC-LH1 protein solution and 5 mM equimolar $K_3[Fe(CN)_6]/K_4[Fe(CN)_6]$ the average forward peak voltage increased to 0.48 V (**Figure 2B**). Supplementary information, **Figure S5** depicts that a control cell with just protein produced ~ 0.25 V voltage response to touch which was three-fold higher than a control cell with just redox electrolyte. This although either the protein alone or electrolyte alone could produce a voltage difference, the strongest effect was seen with both present. The voltage response of devices with proteins increased on increasing the concentration of the redox electrolyte, such that an average forward peak voltage of 1.95 V was observed for 400 mM electrolyte mixed with RC-LH1 in 1:1 ratio (v:v) (**Figure 2C, D**). Although a concentration-dependent increase was seen both in the absence and presence of protein, consistently higher voltages were seen when the redox electrolyte was mixed with the protein (**Figure 2E** and compare Supplementary information **Figure S6 with Figure 2C**). No definite trend was observed in the reverse peak voltage by altering the electrolyte concentration or by adding proteins. The reproducibility of the touch response was demonstrated by applying 150 cycles of touch stimulus and relaxation (**Figure 2F**). A fast response to external pressure (touch) was observed as the distance between the top and bottom electrode reduced significantly and produced a short circuit, resulting in fast electron transport.

The influence of droplet composition was further studied by increasing the redox electrolyte-to-protein volume ratio. A maximum forward peak voltage of 3.29 V (average: 2.52 V) was achieved for the droplet composition of 400 mM electrolyte mixed with RC-LH1 stock solution in 3:1 volume ratio (Supplementary information, **Figure S7**). No further ratio optimization was carried out.

To better understand the role of droplet compression in touch sensing, an apparatus was set up to simultaneously video-record droplet deformation and collect the corresponding electrical response (**Figure 3A**). The bottom electrode was placed on a stage with Z-axis movement control and the top electrode was positioned well above the droplet. Current was measured

continuously as the bottom electrode was raised gradually to a level where the droplet touched the top electrode; sharp peaks of current were observed as the droplet came into contact with the top electrode and began to deform (Supplementary information, **Movie S1**). This confirmed that one of the mechanisms underlying the current and voltage responses to touch is that of an EDLC device[69,71], where the two capacitors formed at either electrode/electrolyte interface charge and discharge with a phase lapse when the droplet is deformed, resulting in a charge transfer from one electrode to the other (**Figure 3B**).

Differential charging and discharging of the two EDLCs is the key phenomenon enabling force-sensing in the device and droplet deformation is a necessary (but not a sufficient) condition for a distinct touch response. As depicted in **Figure 3B**, asymmetric deformation of the droplet with respect to the two electrodes is critical. To prove this, a device configuration with two hydrophobic electrodes was also tested (**Figure 3C**). When the wetting characteristics of the two electrodes were distinctly opposite (**Figure 3D**), sharp current responses were obtained in response to droplet compression (**Figure 3E**) that were two orders of magnitudes higher than obtained with a pair of electrodes of identical (hydrophobic) wetting characteristics (**Figure 3F**). With either configuration the degree of droplet compression had a noticeable effect on the magnitude of the current response; the closer the two electrodes, the higher was the peak current (**Figure 3E, F**). The current response as a function of applied force is shown in Supplementary information, **Figure S8**; a minimum force of 0.9 N was required to trigger a response from the tactile sensor. This indicates that any force applied ≥ 0.9 N will result in an electrical response which can be capitalised for the tactile sensing. Rise and decay times for different applied forces are summarised in **Table S2**.

Photo enhancement in sensing and photo capacitor performance

As seen in **Figure 2B, E**, a pronounced enhancement of the touch-induced voltage signal was achieved with the addition of photoproteins to the redox droplet. As this RC-LH1 protein is known to generate a photocurrent in an electrolyte solution, this enhancement in touch response can be attributed to photochemical reactions in the proteins under the ambient lighting in the laboratory (≈2 W m^{-2} or 0.002 Sun). The reduction potential of the ferricyanide/ferrocyanide electrolyte is intermediate between that of P/P^+ and Q_B/Q_B^- at the poles of a photoexcited protein, and so could mediate both electron and hole flow.

To further examine the efficacy of having the protein present, the touch response was tested in the dark or under ambient light (**Figure 4A**). A touch response of 1.4 V (maximum) in the dark was boosted to 2.1 V (maximum) following exposure to ambient light. Similarly, a photo enhancement of current response was also observed when force was applied on the sensor under 0.3 Sun illumination compared to that under ambient illumination (equivalent to 0.002 Sun) (**Figure 4B)**. When illumination was changed from ambient 0.002 Sun to 0.3 Sun a distinct shift in the baseline current was observed due to the photocurrent response from the proteins (**Figure 4B**, yellow arrow**)**.

The presence of protein had an effect on device performance that was similar to that of a touch stimulus. The protein optically modulated the EDLCs, breaking the equilibrium and increasing the capacitance on one side, while the touch stimulus did the same through mechanical modulation. In the presence of light, the cofactors of the RC domain at the centre of the RC-LH1 protein execute a photo-chemical charge separation process resulting in a net negative charge on one side of the protein at the secondary acceptor ubiquinone (Q_B^- in **Figure 1E** and **S3A**) and a net positive charge on the other at the primary electron donor bacteriochlorophylls (P^+ in **Figure 1E**). The photogenerated electrons from the protein flow towards the ITO-modified Cu bottom electrode, supplementing the positive charge flow towards the top electrode occurring upon touch stimulus (Supplementary information, **Figure S9).** Without any touch stimulus, when there is only an optical stimulus (i.e. illumination) the EDLCs are subjected to a similar equilibrium shift. In the steady state condition (without any mechanical or optical stimulus), the potentials at both EDLCs are the same causing the net device potential to be zero. As the proteins act as a continuous source of photogenerated electrons, directionally flowing towards the bottom electrode and continuously charging the bottom EDLC relative to the top, the device behaves as a photo capacitor (**Figure 4C-G**). Proteins under illumination can be treated as photo-induced dipoles and are known to contribute to the device capacitance[65,73]. In summary therefore, the current/voltage response observed in this work is likely the result of the coexistence of three plausible mechanisms. The first is the formation of an electrochemical double layer at the electrode/electrolyte interface, the second is photoelectrochemical reactions in the protein resulting in photocurrent generation and the third is direct oxidation and reduction of the redox couple electrolyte at the anode and cathode. There is also some probability of direct oxidation or reduction of the protein P^+ or Q_B^- centres by the electrode as the protein is free to diffuse in solution and the P^+ centre in particular is close to the protein surface.

Both the photocurrent generated and the dark discharge time were found be dependent on illumination intensity; for a fixed illumination (charging) period of 30 s, increasing the light intensity from 12 mW cm^{-2} to 100 mW cm^{-2} resulted in a 20-fold increase in the photocurrent density (**Figure 4C, F**). With a fixed intensity of 100 mW cm^{-2} (i.e. 1 Sun), increasing the charging time had a similar effect of increasing the photocurrent density (**Figure 4D, E**). For a photo-charging period of 180 s, the device could generate a photocurrent of 140 µA cm^{-2} which could be trapped in the device even after turning off the light source. The photocurrent slowly decayed to baseline with a long discharge time of >1200 s (**Figure 4D**). A photovoltage of ≈27 mV was generated by the device under 1 Sun illumination and a similar charging and discharging trend was also observed in the voltage scan (**Figure 4G**). Durations taken to stabilise the current response at low (30 mW/cm^2) and high (100 mW/cm^2) light intensities were 148 s and 294 s, respectively. Their respective decay time were 435 s and 1700 s (Supplementary information, **Figure S10**). A longer decay/discharge time is an essential parameter for an efficient photo-capacitor. This has been achieved by modulating the hydrophobicity of the top-ITO electrode to induce slower electron transport and allow charges to be stored within the device. In other words, we reduced the efficiency of the photoelectrochemical cell and turned it into a functional bio-capacitor.

Touch-to-audio conversion

One of the probable applications for this self-powered tactile sensor could be a braille reader that can read out letters of the alphabet corresponding to pixels touched**.** To explore proof-of-concept, the six-pixel tactile sensor was adapted as a touch-to-audio sensor. An electronic interface (See **Note 2, Figure S11** and **S12** in Supplementary Information) comprising a microcontroller and Analog-to-Digital converter was used to collect and digitize the voltage responses from the six pixels of the tactile sensor and translate the digitized voltage signal matrix into a meaningful audio form (**Figure 5A, B**). Focussing on the proposed application, a program code that matched the standard Braille patterns to letters in the 26-character English alphabet was fed to the microcontroller. A Braille pattern comprising six components (in real-life, flat spots and projections but represented in **Figure 5B** by empty and filled circles) can be represented as a matrix of 0's and 1's, where 1's represent the filled circles (equating to Braille projections). When a particular combination of pixels in the sensor was stimulated (**Figure 5B**, top, right) the voltage readings from all the individual pixels were collected by the microcontroller. These were close to 2 V for the stimulated pixels and close to 0 V for those

untouched. The analog voltage matrix was then converted to a matrix of 0's and 1's by the Analog-to-Digital converter. After matching the generated matrix to a letter in the Braille alphabet in the program code, the audio player was triggered by the microcontroller to play an audio pronunciation of the English letter corresponding to the Braille pattern, "I" in the case of the schematic shown in **Figure 5B**. Enacting this, **Figure 5C** illustrates and Supplementary information **Movies S2 and S3** demonstrate touch-to-audio conversion for seven different Braille letters "A", "B", "C", "I", "K", "U" and "V", corresponding to one, two, three and four pixels.

Conclusions

In summary, in contrast to most reported tactile sensors that either stop at quantification of the sensory data in terms of an electrical signal such as voltage, resistance or capacitance, or return a visual feedback in response to a touch stimulus, in this report the concept of touch-to-audio translation is demonstrated. The proof-of-concept device aims to address two major shortcomings in the field: (1) the lack of device models with non-visual sensory feedbacks and (2) the lack of sustainable, hazard-free sources of continuous, non-pulsated power-supply that could be integrated into the sensors. The presented model could particularly be of value to visually impaired (or partially sighted) children and adults in learning and reading Braille text, and sharing the sensory input with others. The improvement of Braille literacy and the ease of reading Braille is very relevant even today, but is not well-researched. New efforts are being taken to improve Braille literacy, with for example the toy manufacturer The LEGO Group (Billund, Denmark) having recently launched Braille bricks to enhance Braille learning among visually impaired children[74]. The touch-to-audio tactile sensor model presented here could be a valuable contribution in this area if e-Braille readers can be developed as wearable- or on-skin devices enabling the user to hear the audio corresponding to the Braille text they touch. With device miniaturization and the use of more sophisticated microfluidic fabrication routes, the presented model could potentially find application in future electronic gadgets for the visually impaired. It also demonstrates a new way to exploit the solar energy harvesting, conversion and storage capacities of natural photosynthetic pigment-proteins in a sensing device.

Materials and Methods

Biological Material. The RC-LH1 protein was purified from a PufX-deficient strain of *Rba. sphaeroides* as described previously[60]. It was stored at -80°C as a concentrated solution in 20 mM Tris (pH 8.0)/0.04% (w/v) n-dodecyl β-D-maltopyranoside. The concentration of protein was such that the absorbance at 875 nm was equivalent to ~380 absorbance units cm^{-1}.

Materials. The PDMS used was Sylgard 184 from Dow Corning, along with its silicone elastomer curing agent. The mould used to cast the PDMS base with wells was 3D-printed with ABS polymer. ITO/PET sheets, glacial acetic acid, 1H,1H,2H,2H-perfluorodecyltriethoxysilane (97%) (PFDTS), potassium ferrocyanide ($K_4[Fe(CN)_6]$), and potassium ferricyanide ($K_3[Fe(CN)_6]$) were procured from Sigma Aldrich. The ethanol used was EMSURE® ACS, ISO, Reag. Ph Eur Ethanol from EMD Millipore Corporation. The 2-propanol used was the Baker Analyzed® ACS Reagent of Avantor Performance Materials, Inc. Strips of 3M™ copper foil (0.101mm) were used for bottom electrodes.

Contact Angle Measurement. Contact angle were measured using an AST Products VCA Optima XE Contact Angle Goniometer using a 5 μL water droplet at r.t.p. Measurements were taken 1-2 minutes after the droplet had been deposited and was adhered to the sample surface. The contact angle of each sample was determined by taking the average of contact angles obtained at different points on the sample surface.

Fabrication of bottom electrode. Strips of copper tape were carefully cut and each was adhered onto one of the protrusions on the ABS mould (shown in Supplementary information, **Figure S1B**). After mixing the curing agent and base PDMS polymer at a 1:10 weight ratio, the mixture was poured and filled into the ABS mould up to a thickness of ~2.5 mm. The mould was placed in an oven and the PDMS cured at a temperature of 70-80°C for ~3.5 hours. The shaped PDMS base was then manually peeled from the mould and was covered with a mask for ITO sputtering, comprising thick paper with square holes to prevent ITO covering the cavities. The PDMS base was then placed inside the chamber of a Discovery® 18 Sputtering System (Denton) and ITO was sputtered for 20 minutes at a RF power of 128 Watts using 99.99% ITO target (Angstrom Sciences). A thin ITO film (≈200 nm) was deposited on the surface of the copper foil located at the bottom of each of the six cavities in the shaped PDMS.

Fabrication of top electrode. An ITO/PET (ITO film coated on PET) sheet treated with PFDTS was used as the top electrode. Two solutions, one of 1:10 (v/v) ratio of PFDTS and ethanol (Solution 1) and the other of 1 wt.% acetic acid in propanol (Solution 2) were prepared. A few drops of Solution 2 were poured onto the ITO side of the ITO/PET sheet and left for 10

minutes. The sheet was then heated at ~100°C for 1 hour. Following the heating step the ITO/PET sheet was immersed in Solution 1 for 1 hour, was dried at r.t.p. for 24 hours and then rinsed with deionized water. Four similar protocols were explored to optimize the wetting characteristics of the top electrode (See **Note 1,** Supplementary Information The top and bottom electrodes were assembled to obtain the final device. The dimensional parameters are elaborated in supplementary information, **Figure S13.** The height of the 3 µL protein + redox droplet for all sensing measurements was maintained at ~1.2 mm with the depth of the braille cell of ~2 mm.

Preparation of ionic droplets. Separate 1 M stock solutions of $K_3[Fe(CN)_6]$ and $K_4[Fe(CN)_6]$ were prepared using deionized water as the solvent. Equimolar solutions of $K_3[Fe(CN)_6]/K_4[Fe(CN)_6]$ of four different concentrations (5 mM, 10 mM, 0.1 M, and 0.4 M) were prepared by mixing and diluting the stock solutions. For device configurations with 'redox + protein' droplets, a concentrated stock solution of RC-LH1 protein was mixed with one of the four prepared solutions of $K_3[Fe(CN)_6]/K_4[Fe(CN)_6]$ in a 1:1 or 1:3 (Redox mediator: Protein = 3:1) volume ratio.

Electrical measurements for tactile sensing and photo capacitor performance: A Keithley 2450 Source meter was to measure the current and voltage scans against time for testing both the tactile sensing characteristics and photo-capacitor performance. For all tactile sensing experiments the force applied on the sensor was ~7.84 N. Given the application of Braille sensing which required only binary readings (i.e. 'touch' = 1 and 'no touch = 0), no detailed studies on pressure/force sensitivity were conducted. For all photo capacitor measurements, including photocurrent and photovoltage measurements, a tungsten-halogen lamp was used as the light source; the active area of illumination was ≈0.05 cm^2. Light intensity was controlled by varying the sample-to-lamp distance and was measured using a Newport irradiance meter.

Real-time monitoring of droplet compression and electrical response. The experimental setup used for the simultaneous recording of droplet compression and electrical response is shown in **Figure 3A**. A micro-syringe was used to place a 3 µL droplet on the bottom electrode after the setup has been constructed. The two electrodes were connected to a Keithley 2450 Source meter. A CCD camera (VCA Optima) was used to capture a real-time video of the droplet being compressed (brought about by moving the stage with Z-axis control on which the bottom electrode was rested). The camera was connected to a computer, and the related software (VCA Optima EX) was used to display the real-time video on the monitor. As the camera recorded the droplet compression a second camera was used to simultaneously record

the electric response displayed on the screen of the Keithley 2450 Source meter. Example data are shown in Supplementary information **Movie S1**.

Electronic Supplementary Information

References and Notes

1 Pu, X. *et al.* Eye motion triggered self-powered mechnosensational communication system using triboelectric nanogenerator. *Science advances* **3**, e1700694 (2017).
2 Lee, Y., Cha, S. H., Kim, Y.-W., Choi, D. & Sun, J.-Y. Transparent and attachable ionic communicators based on self-cleanable triboelectric nanogenerators. *Nature communications* **9**, 1804 (2018).

3 Dong, W., Huang, Y., Yin, Z., Zhou, Y. & Chen, J. in *International Conference on Intelligent Robotics and Applications.* 155-163 (Springer).
4 Liu, Y. *et al.* Epidermal mechano-acoustic sensing electronics for cardiovascular diagnostics and human-machine interfaces. *Science Advances* **2**, e1601185 (2016).
5 Kim, J., Campbell, A. S., de Avila, B. E. & Wang, J. Wearable biosensors for healthcare monitoring. *Nature Biotechnology* **37**, 389-406, doi:10.1038/s41587-019-0045-y (2019).
6 Akhtar, A., Sombeck, J., Boyce, B. & Bretl, T. Controlling sensation intensity for electrotactile stimulation in human-machine interfaces. *Science Robotics* **3**, eaap9770 (2018).
7 Tucker, A. in *Virtual Weaponry* 69-105 (Springer, 2017).
8 Aaltonen, I. & Laarni, J. Field evaluation of a wearable multimodal soldier navigation system. *Applied ergonomics* **63**, 79-90 (2017).
9 Naujoks, F., Forster, Y., Wiedemann, K. & Neukum, A. 585-595 (Springer International Publishing).
10 Chandarana, M., Trujillo, A., Shimada, K. & Danette Allen, B. 387-398 (Springer International Publishing).
11 Huang, Z. *et al.* Three-dimensional integrated stretchable electronics. *Nature Electronics* **1**, 473 (2018).
12 Rich, S. I., Wood, R. J. & Majidi, C. Untethered soft robotics. *Nature Electronics* **1**, 102 (2018).
13 Lamkin, P. *Smart Wearables Market To Double By 2022: $27 Billion Industry Forecast*, <https://www.forbes.com/sites/paullamkin/2018/10/23/smart-wearables-market-to-double-by-2022-27-billion-industry-forecast> (2018).
14 Wang, S. *et al.* Skin electronics from scalable fabrication of an intrinsically stretchable transistor array. *Nature* **555**, 83 (2018).
15 Dai, Y. *et al.* A Self-Powered Brain-Linked Vision Electronic-Skin Based on Triboelectric-Photodetecing Pixel-Addressable Matrix for Visual-Image Recognition and Behavior Intervention. *Advanced Functional Materials* **28**, 1800275 (2018).
16 Hua, Q. *et al.* Skin-inspired highly stretchable and conformable matrix networks for multifunctional sensing. *Nature Communications* **9**, 244, doi:10.1038/s41467-017-02685-9 (2018).
17 Someya, T. & Amagai, M. Toward a new generation of smart skins. *Nature Biotechnology* **37**, 382-388, doi:10.1038/s41587-019-0079-1 (2019).
18 Wang, J., Lin, M.-F., Park, S. & Lee, P. S. Deformable conductors for human–machine interface. *Materials Today* **21**, 508-526, doi:https://doi.org/10.1016/j.mattod.2017.12.006 (2018).
19 Park, J., Kim, M., Lee, Y., Lee, H. S. & Ko, H. Fingertip skin–inspired microstructured ferroelectric skins discriminate static/dynamic pressure and temperature stimuli. *Science Advances* **1**, e1500661 (2015).
20 Boutry, C. M. *et al.* A stretchable and biodegradable strain and pressure sensor for orthopaedic application. *Nature Electronics* **1**, 314-321, doi:10.1038/s41928-018-0071-7 (2018).
21 Yin, B., Liu, X., Gao, H., Fu, T. & Yao, J. Bioinspired and bristled microparticles for ultrasensitive pressure and strain sensors. *Nature Communications* **9**, 5161, doi:10.1038/s41467-018-07672-2 (2018).

22 Chortos, A. & Bao, Z. Skin-inspired electronic devices. *Materials Today* **17**, 321-331, doi:https://doi.org/10.1016/j.mattod.2014.05.006 (2014).
23 Tian, R., Liu, Y., Koumoto, K. & Chen, J. Body Heat Powers Future Electronic Skins. *Joule* **3**, 1399-1403, doi:10.1016/j.joule.2019.03.011 (2019).
24 Guo, H. *et al.* A highly sensitive, self-powered triboelectric auditory sensor for social robotics and hearing aids. *Science Robotics* **3**, eaat2516 (2018).
25 Wu, Y. *et al.* A skin-inspired tactile sensor for smart prosthetics. *Science Robotics* **3**, eaat0429 (2018).
26 Osborn, L. E. *et al.* Prosthesis with neuromorphic multilayered e-dermis perceives touch and pain. *Science Robotics* **3**, eaat3818 (2018).
27 Hong, S. Y. *et al.* Polyurethane foam coated with a multi-walled carbon nanotube/polyaniline nanocomposite for a skin-like stretchable array of multi-functional sensors. *NPG Asia Materials* **9**, doi:10.1038/am.2017.194 (2017).
28 Miyamoto, A. *et al.* Inflammation-free, gas-permeable, lightweight, stretchable on-skin electronics with nanomeshes. *Nature Nanotechnology* **12**, 907 (2017).
29 Suresh, L. *et al.* High-Performance UV Enhancer Molecules Coupled with Photosynthetic Proteins for Ultra-Low-Intensity UV Detection. *Chem* **5**, 1847-1860, doi:https://doi.org/10.1016/j.chempr.2019.04.017 (2019).
30 Yokota, T. *et al.* Ultraflexible organic photonic skin. *Science Advances* **2**, doi:10.1126/sciadv.1501856 (2016).
31 An, B. W., Heo, S., Ji, S., Bien, F. & Park, J. U. Transparent and flexible fingerprint sensor array with multiplexed detection of tactile pressure and skin temperature. *Nature Communications* **9**, 2458, doi:10.1038/s41467-018-04906-1 (2018).
32 Sarwar, M. S. *et al.* Bend, stretch, and touch: Locating a finger on an actively deformed transparent sensor array. *Science Advances* **3**, e1602200 (2017).
33 Jung, S. *et al.* Reverse-Micelle-Induced Porous Pressure-Sensitive Rubber for Wearable Human–Machine Interfaces. *Advanced Materials* **26**, 4825-4830, doi:10.1002/adma.201401364 (2014).
34 Han, S. *et al.* Battery-free, wireless sensors for full-body pressure and temperature mapping. *Science Translational Medicine* **10**, eaan4950 (2018).
35 Zang, Y. *et al.* Flexible suspended gate organic thin-film transistors for ultra-sensitive pressure detection. *Nature Communications* **6**, 6269, doi:10.1038/ncomms7269

https://www.nature.com/articles/ncomms7269#supplementary-information (2015).
36 Zhang, Y. *et al.* Performance and service behavior in 1-D nanostructured energy conversion devices. *Nano Energy* **14**, 30-48 (2015).
37 Wu, W. & Wang, Z. L. Piezotronics and piezo-phototronics for adaptive electronics and optoelectronics. *Nature Reviews Materials* **1**, 16031 (2016).
38 Zhang, Y. *et al.* Scanning probe study on the piezotronic effect in ZnO nanomaterials and nanodevices. *Advanced Materials* **24**, 4647-4655 (2012).
39 Wu, W., Wen, X. & Wang, Z. L. Taxel-addressable matrix of vertical-nanowire piezotronic transistors for active/adaptive tactile imaging. *Science* **340**, 1234855 (2013).
40 Pu, X. *et al.* Ultrastretchable, transparent triboelectric nanogenerator as electronic skin for biomechanical energy harvesting and tactile sensing. *Science Advances* **3**, e1700015, doi:10.1126/sciadv.1700015 (2017).

41 Khan, U., Kim, T.-H., Ryu, H., Seung, W. & Kim, S.-W. Graphene Tribotronics for Electronic Skin and Touch Screen Applications. *Advanced Materials* **29**, 1603544-n/a, doi:10.1002/adma.201603544 (2017).
42 Ravi, S. K. *et al.* Optical Shading Induces an In-Plane Potential Gradient in a Semiartificial Photosynthetic System Bringing Photoelectric Synergy. *Advanced Energy Materials* **9**, 1901449, doi:10.1002/aenm.201901449 (2019).
43 Takei, K. *et al.* Nanowire active-matrix circuitry for low-voltage macroscale artificial skin. *Nature Materials* **9**, 821-826, doi:http://www.nature.com/nmat/journal/v9/n10/abs/nmat2835.html#supplementary-information (2010).
44 Shin, S.-H. *et al.* Integrated arrays of air-dielectric graphene transistors as transparent active-matrix pressure sensors for wide pressure ranges. *Nature communications* **8**, 14950 (2017).
45 Zhang, F., Zang, Y., Huang, D., Di, C. A. & Zhu, D. Flexible and self-powered temperature-pressure dual-parameter sensors using microstructure-frame-supported organic thermoelectric materials. *Nature Communications* **6**, 8356, doi:10.1038/ncomms9356 (2015).
46 Wang, X. *et al.* Self-powered high-resolution and pressure-sensitive triboelectric sensor matrix for real-time tactile mapping. *Advanced Materials* **28**, 2896-2903 (2016).
47 Gerratt, A. P., Michaud, H. O. & Lacour, S. P. Elastomeric electronic skin for prosthetic tactile sensation. *Advanced Functional Materials* **25**, 2287-2295 (2015).
48 Son, D. *et al.* An integrated self-healable electronic skin system fabricated via dynamic reconstruction of a nanostructured conducting network. *Nature Nanotechnology* **13**, 1057 (2018).
49 Freeman, E. *et al.* Interaction techniques with novel multimodal feedback for addressing gesture-sensing systems}}. 115-119 (2016).
50 Morrison, C., Smyth, N., Corish, R., O'Hara, K. & Sellen, A. in *Proceedings of the 2014 conference on Designing interactive systems.* 229-238 (ACM).
51 Ravi, S. K. *et al.* A Mechanoresponsive Phase-Changing Electrolyte Enables Fabrication of High-Output Solid-State Photobioelectrochemical Devices from Pigment-Protein Multilayers. *Advanced Materials* **30**, 1704073 (2018).
52 Yehezkeli, O. *et al.* Integrated photosystem II-based photo-bioelectrochemical cells. *Nature Communications* **3**, 742, doi:10.1038/ncomms1741 (2012).
53 Efrati, A. *et al.* Assembly of photo-bioelectrochemical cells using photosystem I-functionalized electrodes. *Nature Energy* **1**, 15021 (2016).
54 Mirvakili, S. M. *et al.* Photoactive Electrodes Incorporating Electrosprayed Bacterial Reaction Centers. *Advanced Functional Materials* **24**, 4789-4794, doi:10.1002/adfm.201400350 (2014).
55 Ham, M.-H. *et al.* Photoelectrochemical complexes for solar energy conversion that chemically and autonomously regenerate. *Nature Chemistry* **2**, 929-936 (2010).
56 den Hollander, M.-J. *et al.* Enhanced Photocurrent Generation by Photosynthetic Bacterial Reaction Centers through Molecular Relays, Light-Harvesting Complexes, and Direct Protein-Gold Interactions. *Langmuir* **27**, 10282-10294, doi:10.1021/la2013528 (2011).

57 Swainsbury, D. J., Friebe, V. M., Frese, R. N. & Jones, M. R. Evaluation of a biohybrid photoelectrochemical cell employing the purple bacterial reaction centre as a biosensor for herbicides. *Biosensors and Bioelectronics* **58**, 172-178 (2014).
58 Yaghoubi, H. *et al.* Hybrid Wiring of the Rhodobacter sphaeroides Reaction Center for Applications in Bio-photoelectrochemical Solar Cells. *The Journal of Physical Chemistry C* **118**, 23509-23518 (2014).
59 Caterino, R. *et al.* Photocurrent generation in diamond electrodes modified with reaction centers. *ACS applied materials & interfaces* **7**, 8099-8107 (2015).
60 Friebe, V. M. *et al.* Plasmon-Enhanced Photocurrent of Photosynthetic Pigment Proteins on Nanoporous Silver. *Advanced Functional Materials* **26**, 285-292 (2016).
61 Yaghoubi, H. *et al.* Large Photocurrent Response and External Quantum Efficiency in Biophotoelectrochemical Cells Incorporating Reaction Center Plus Light Harvesting Complexes. *Biomacromolecules* **16**, 1112-1118 (2015).
62 Das, R. *et al.* Integration of photosynthetic protein molecular complexes in solid-state electronic devices. *Nano Letters* **4**, 1079-1083, doi:10.1021/nl049579f (2004).
63 Ravi, S. K. & Tan, S. C. Progress and perspectives in exploiting photosynthetic biomolecules for solar energy harnessing. *Energy & Environmental Science* **8**, 2551-2573 (2015).
64 Ravi, S. K., Udayagiri, V. S., Suresh, L. & Tan, S. C. Emerging Role of the Band-Structure Approach in Biohybrid Photovoltaics: A Path Beyond Bioelectrochemistry. *Advanced Functional Materials* **28**, 1705305 (2018).
65 Singh, V. K. *et al.* Biohybrid Photoprotein-Semiconductor Cells with Deep-Lying Redox Shuttles Achieve a 0.7 V Photovoltage. *Advanced Functional Materials* **28**, 1703689, doi:10.1002/adfm.201703689 (2018).
66 Suresh, L., Vaghasiya, J. V., Jones, M. R. & Tan, S. C. Biodegradable Protein-Based Photoelectrochemical Cells with Biopolymer Composite Electrodes That Enable Recovery of Valuable Metals. *ACS Sustainable Chemistry & Engineering* **7**, 8834-8841, doi:10.1021/acssuschemeng.9b00790 (2019).
67 Vaghasiya, J. V., Nandakumar, D. K., Yaoxin, Z. & Tan, S. C. Low toxicity environmentally friendly single component aqueous organic ionic conductors for high efficiency photoelectrochemical solar cells. *Journal of Materials Chemistry A* **6**, 1009-1016, doi:10.1039/C7TA09557K (2018).
68 Ravi, S. K. *et al.* Photosynthetic Bioelectronic Sensors for Touch Perception, UV-Detection, and Nanopower Generation: Toward Self-Powered E-Skins. *Advanced Materials* **30**, 1802290 (2018).
69 Liu, K. *et al.* Self-Powered Multimodal Temperature and Force Sensor Based-On a Liquid Droplet. *Angewandte Chemie International Edition* **55**, 15864-15868 (2016).
70 Nie, B., Xing, S., Brandt, J. D. & Pan, T. Droplet-based interfacial capacitive sensing. *Lab on a Chip* **12**, 1110-1118 (2012).
71 Moon, J. K., Jeong, J., Lee, D. & Pak, H. K. Electrical power generation by mechanically modulating electrical double layers. *Nature Communications* **4**, 1487, doi:10.1038/ncomms2485

https://www.nature.com/articles/ncomms2485#supplementary-information (2013).
72 Nie, B., Li, R., Brandt, J. D. & Pan, T. Microfluidic tactile sensors for three-dimensional contact force measurements. *Lab on a Chip* **14**, 4344-4353, doi:10.1039/C4LC00746H (2014).

73 Ravi, S. K. *et al.* Photosynthetic apparatus of Rhodobacter sphaeroides exhibits prolonged charge storage. *Nature communications* **10**, 902 (2019).
74 Mervosh, S. in *The New York Times* (April 27, 2019).

Acknowledgments

Funding: S.C.T. acknowledges financial support from MOE AcRF 1 (R-284-000-161-114). M.R.J. acknowledges support from the Biotechnology and Biological Sciences Research Council (BBSRC—project BB/I022570/1) and the BrisSynBio Synthetic Biology Research Centre at the University of Bristol (BB/L01386X/1) funded by the BBSRC and the Engineering and Physical Sciences Research Council (EPSRC) of the UK.

Author contributions:

S.K.R. and S.C.T. conceived the concept presented and designed the experiments. S.K.R and A.T.S tested the tactile sensing characteristics of the sensor. A.T.S performed experiments on optimizing the device design and droplet composition. S.K.R tested the photo capacitive behavior of the sensors. T.W. designed the electronic interface. Z. W. assisted in the preliminary studies on selection of electrolytes and electrolyte synthesis. M.R.J. provided the biological materials. L.S. and N.P. performed confirmatory experiments and assisted in manuscript revisions. S.K.R., L.S., A.T.S., M.R.J. and S.C.T. analyzed and interpreted the data and wrote the manuscript. S.C.T. supervised the project.

Competing interests: The authors declare that they have no competing interests.

Data and materials availability: All data needed to evaluate the conclusions in the paper are present in the paper and/or the Supplementary Materials. Additional data related to this paper may be requested from the authors.

Figures

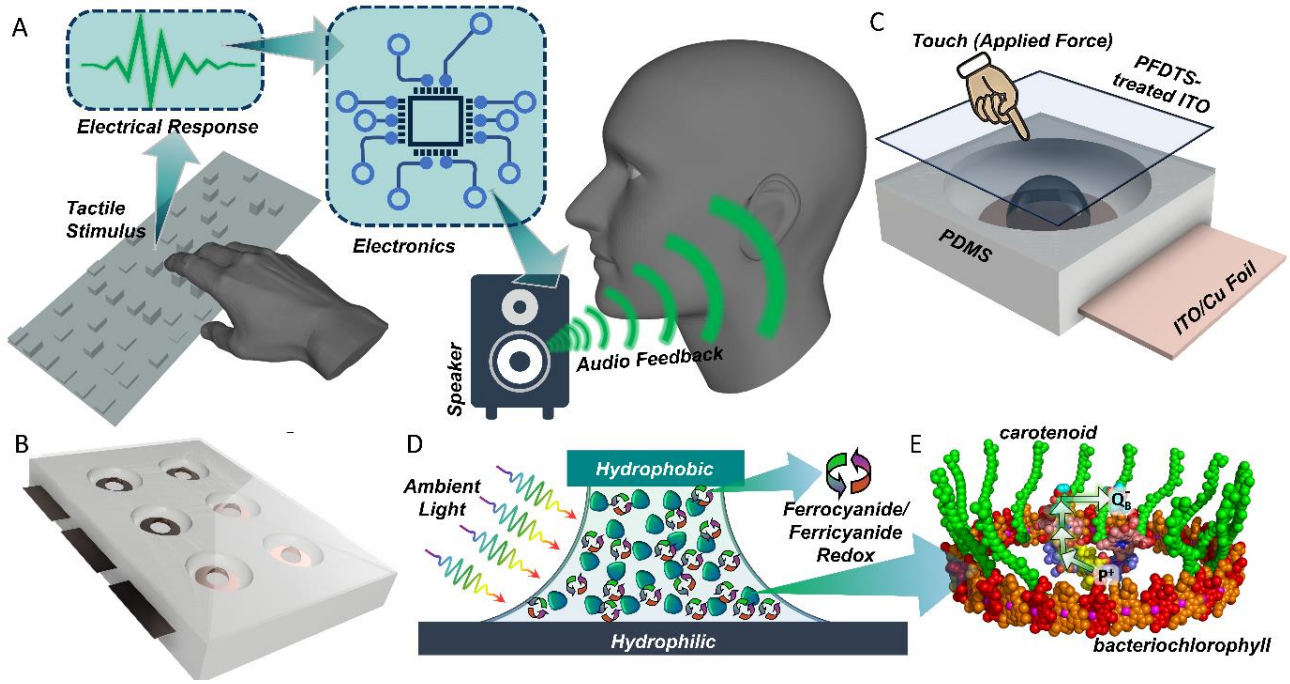

Figure 1: Concept of touch-to-audio conversion and device design. (**A**) Cartoon showing the concept of perceiving a textured/patterned surface by touch through an audio feedback. (**B**) Six-pixel tactile sensor with an ionic droplet in each pixel (see **Figure S1** for a summary of device fabrication). (**C**) Components of a single pixel. (**D**) Optical and mechanical modulation of a bio-electrochemical liquid bridge composed of a redox electrolyte and photosynthetic proteins between electrodes of opposite wetting characteristics. (**E**) Arrangement of the

cofactor system of the RC-LH1 protein for light capture and photochemical charge separation (arrows).

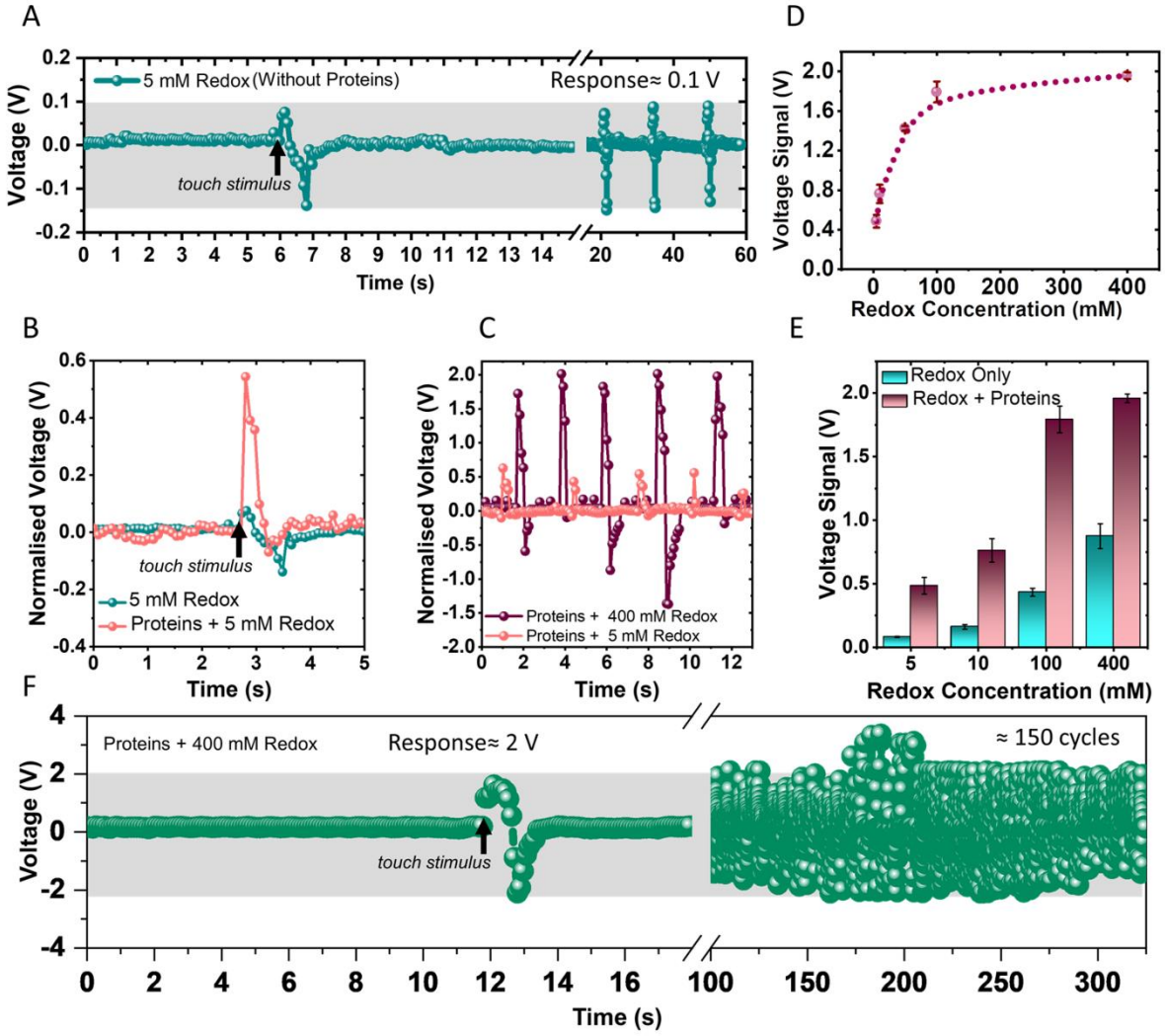

Figure 2: Tactile sensing characteristics and effects of droplet composition. (A) Touch response for a droplet with 5 mM redox electrolyte without protein addition; shading shows the mode-to-mode response range. (**B**) Enhancement of touch response by addition of proteins to 5 mM redox electrolyte. (**C, D**) Effect of redox electrolyte concentration on touch response in 'protein + redox' devices showing reproducibility (C) and mean maximum voltage signal (D). (**E**) Effect of redox electrolyte concentration in redox-only and redox + protein devices. (**F**) Reproducibility of touch responses with 150 cycles of stimulus for a redox + protein device with 400 mM redox electrolyte.

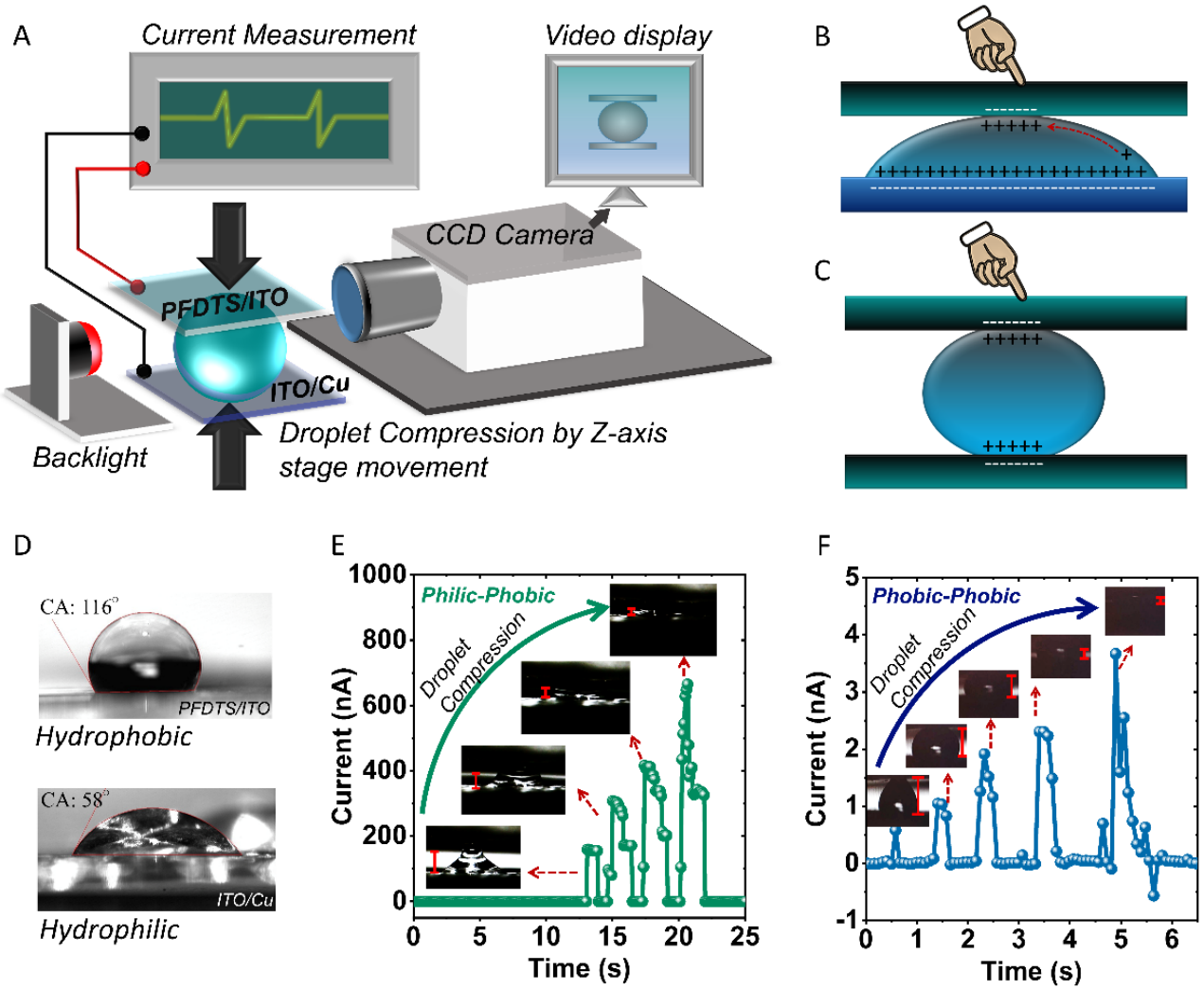

Figure 3: Real-time monitoring of liquid bridge modulation and electrical response. (A) Apparatus for simultaneous recording of droplet compression and current measurement (see **Supplementary Movie S1**). (**B**) Device configuration under compression with a hydrophilic bottom electrode and a hydrophobic top electrode. **(C)** Device configuration under compression with two hydrophobic electrodes. (**D**) Wetting characteristics of the two electrode materials – PFDTS-treated ITO gave a contact angle (CA) of 116° (i.e. hydrophobic) and ITO-modified Cu gave a contact angle of 58° (i.e. hydrophilic). **(E, F)** Effect of increasing droplet compression on the current response for a hydrophilic-hydrophobic electrode configuration (E) and a hydrophobic-hydrophobic electrode configuration (F).

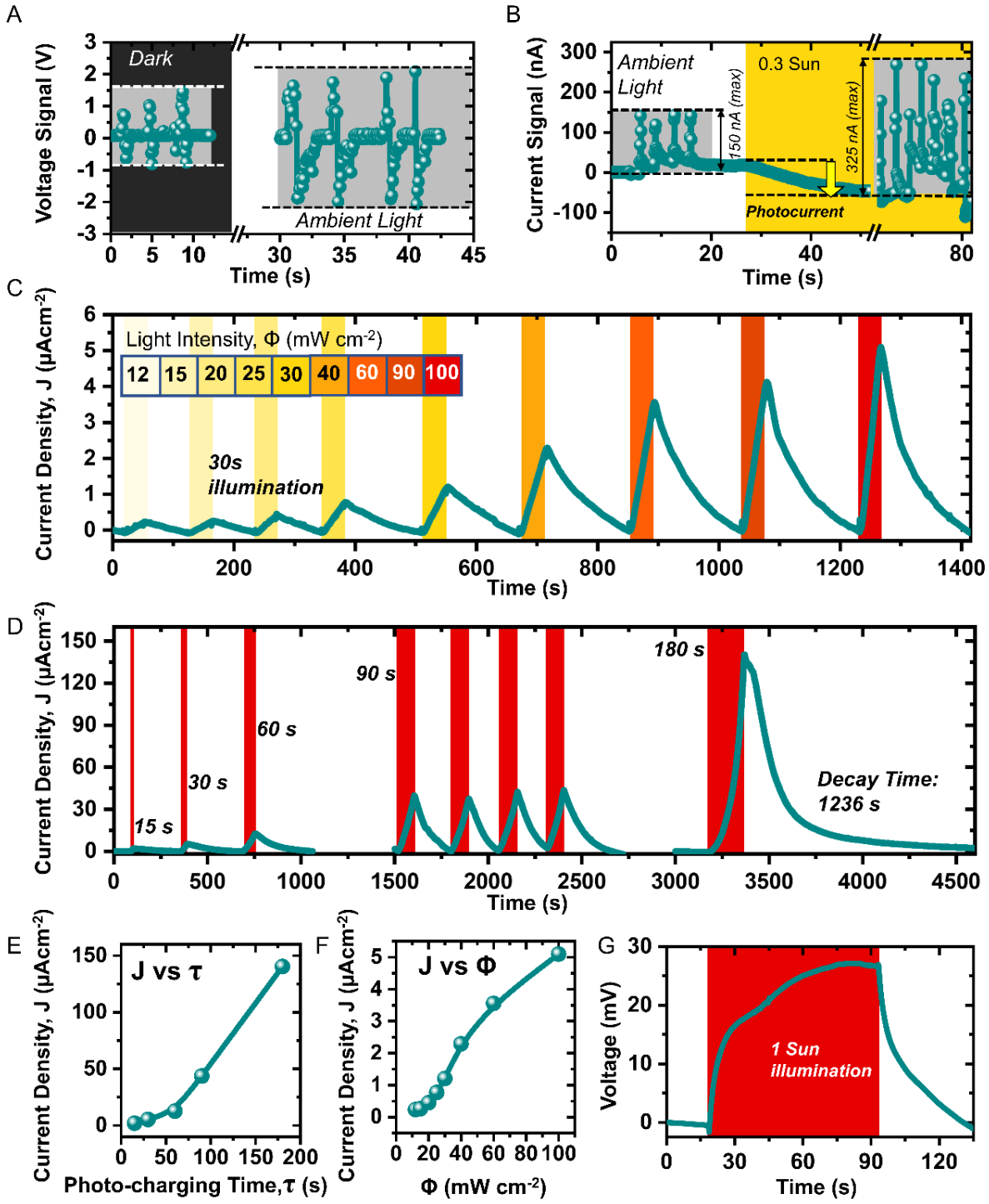

Figure 4: Photo-enhancement of tactile sensing and bio-photocapacitive performance. All data are for a protein + 400 mM redox electrolyte device. **(A)** Enhancement of touch response by ambient light. **(B)** Effect of increased illumination on touch response and current baseline. **(C)** Photo-charging for 30 s at nine different light intensities (Φ). **(D)** Photocurrent generation with charging and discharging trends for different illumination periods (photo-charging charging time); ≈180s of photo-charging by 1 Sun illumination (equivalent to 100 mW cm^{-2}). resulted in a 6.5-fold longer discharge time. **(E)** Effect of photo-charging time (**τ**) on photocurrent density. **(F)** Effect of light intensity (Φ) on the photocurrent density reached at the end of 30 s photo-charging. **(G)** Photovoltage generation under 75 s of 1 Sun illumination.

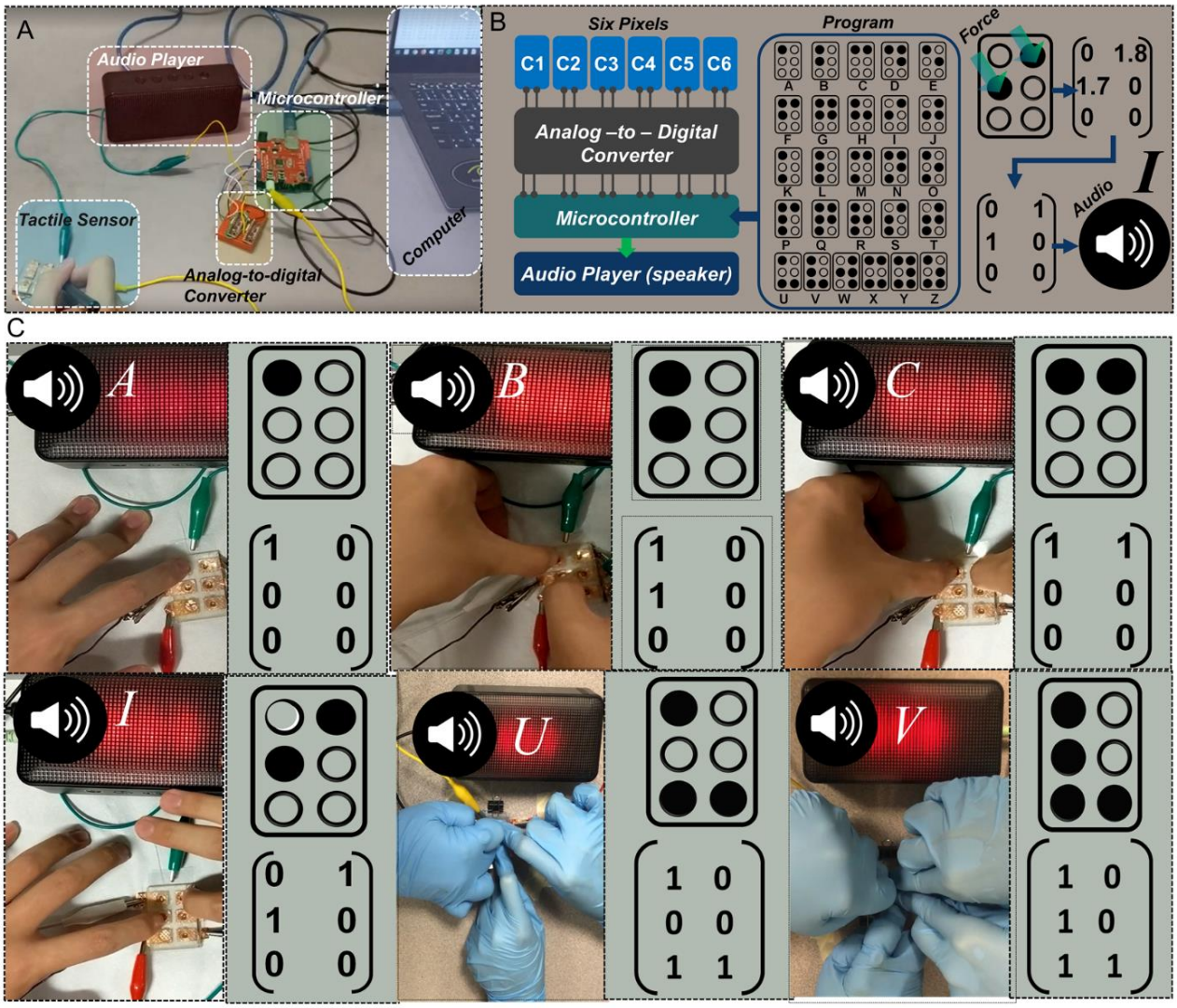

Figure 5: Demonstration of touch-to-audio conversion. (A) Summary of apparatus used for translating a touch stimulus to audio feedback. **(B)** Schematic of the electronic interface used to convert touch stimuli of a six-pixel sensor in a particular Braille pattern to a meaningful audio pronunciation using a program that matches a Braille pattern each to a letter in the English alphabet. In the example shown touching two of the pixels results in voltages being recorded (1.8 V in one and 1.7 V in the other) alongside near-zero base voltages in the remaining four. This is digitized into a matrix of 0's and 1's that matches a particular Braille pattern, triggering the audio player to pronounce the corresponding letter ("*I*" in this case) which is heard by the user. **(C)** Snapshots from a touch-to-audio demonstration converting different Braille patterns to audio signals (see **Supplementary Movie S2 and S3**)